Title

Atomic autoionization in the photo-dissociation of super-excited deuterated water molecules fragmenting into D + + O + + D

Journal

Physical Chemistry Chemical Physics, 25(32)

ISSN

1463-9076

Authors

Iskandar, W
Rescigno, TN
Orel, AE
et al.

Publication Date

2023-08-16

DOI

10.1039/d3cp02438e

Peer reviewed

PCCP

ARTICLE TYPE

Cite this: DOI: 00.0000/xxxxxxxxxx

Atomic autoionization in the photo-dissociation of super-excited deuterated water molecules fragmenting into $D^+ + O^+ + D$

W. Iskandar,[a] T.N. Rescigno,[a†] A.E. Orel,[b] K.A. Larsen,[a,c] B. Griffin,[a,d] D. Call,[d], V. Davis,[d] B. Jochim, [e] T. Severt,[e] J.B. Williams,[d] I. Ben-Itzhak,[e] D.S. Slaughter, [a] and Th. Weber [a‡]

Received Date
Accepted Date

DOI: 00.0000/xxxxxxxxxx

We present the relaxation dynamics of deuterated water molecules via autoionization, initiated by the absorption of a 61 eV photon, producing the very rare $D^+ + O^+ + D$ breakup channel. We employ the COLd Target Recoil Ion Momentum Spectroscopy method to measure the 3D momenta of the ionic fragments and emitted electrons from the dissociating molecule in coincidence. We interpret the results using the potential energy surfaces extracted from multi-reference configuration interaction calculations. The measured particle energy distributions can be related to a super-excited monocationic state located above the double ionization threshold of D_2O. The autoionized electron energy shows a sharp distribution centered around 0.5 eV, which is a signature of the atomic oxygen autoionization occurring in the direct and sequential dissociation processes of D_2O^{+*} at a large internuclear distance. In this way, an O^+ radical fragment and a low-energy electron are created, both of which can trigger secondary reactions in their environment.

1 Introduction

Detailed insight into elemental light-matter interactions of water molecules is not only important to advance fundamental research but also indispensable to drive forward fields as diverse as radio-biology and astrophysics[1,2]. This is because water is very common in nature, and its response to radiation can determine the fate of bio-molecules[1] or cause chemical reactions in planetary atmospheres[2]. This is especially the case when excited electronic states are populated and low-energy electrons are generated throughout the dissociation process. Such low-energy electrons can trigger secondary reactions, e.g., dissociative electron attachment to neighboring DNA molecules which can cause (double) strand breakage[3]. While water has been studied extensively in the past, the observation of radical atoms, ions and electrons formed after photoionization and excitation as well as the identification of all relaxation steps in the subsequent single- or multi-step dissociation process leading to those fragments is still a challenge for theory and experiment alike.

Single-photon double ionization of water is generally followed by the fragmentation of the dication. Non-dissociative water dications have never been observed; only fragments of the dication have been detected. These fragments can be produced via direct double ionization after absorption of the photon[4], where two electrons are emitted simultaneously, or via indirect double ionization (IDI) processes, in which electrons are expelled during subsequent dissociation steps[4,5]. The latter fragmentation routes have been the subject of various highly differential investigations in the past. Prior results on the photo-double ionization (PDI) of H_2O using photon energies of 43 eV identified a sequential fragmentation process which included autoionization[5]. In this sequence, the neutral water molecules were first singly ionized and simultaneously excited, before they subsequently dissociated into a proton and an autoionizing OH^* fragment, which eventually lead to the detected $H^+ + OH^+$ products. More recent studies targeted the PDI of H_2O at a higher photon energy of around 57 eV[4]. The same molecular autoionization pathway as in Sann *et al.*[5], which lead to the two-body fragmentation $H^+ + OH^+$, while producing an autoionized electron of near-zero energy, was identified and played a major part in the PDI. The latter study also investigated the three-body fragmentation channel $H^+ + H^+ + O$, but no traces of autoionization were found to contribute to this breakup. Due to the limited statistics in this experiment, which is prohibitive of (highly-) differential studies, the $H^+ + O^+ + H$ breakup channel was not identified and could not be investigated.

In the present state-selective highly-differential investigation of the PDI of D_2O molecules, using single photons with 61 eV, we

[a] Chemical Sciences Division, Lawrence Berkeley National Laboratory, Berkeley, CA-94720, USA
[b] Chemical Engineering of California, Davis, CA-95616, USA
[c] Graduate Group in Applied Science and Technology, Berkeley, CA-94720, USA
[d] Department of Physics, University of Nevada, Reno, NV-89557, USA
[e] J. R. Macdonald Laboratory, Department of Physics, Kansas State University, Manhattan, KS-66506, USA
E-Mail: † TNRescigno@lbl.gov, † TWeber@lbl.gov

now identify and trace two competing reaction processes leading to the rare $D^+ + O^+ + D$ three-body breakup of this triatomic molecule. This fragmentation route originates from an excited D_2O^{+*} monocation whose internal energy exceeds the double ionization potential, i.e. it resides in the D_2O^{2+} continuum. This intermediate super-excited state of the deuterated water molecular ion is highly unstable and decays through atomic O^* autoionization, while having the potential to produce a very low-energy electron at large internuclear distances. These slow electrons are then able to initiate (i.a., harmful) secondary reactions in the local environment. In this process, the water monocation can dissociate directly or sequentially, which we can distinguish experimentally and trace with the help of Multi Reference Configuration Interaction (MRCI) calculations. Moreover, the branching ratios of these different dissociation pathways can be determined, while additional experimental insights are made by employing the native-frames analysis[6,7] and performing Monte-Carlo simulations.

2 Experiment

The experiments were performed at the undulator beamline 10.0.1.3 of the Advanced Light Source (ALS) at Lawrence Berkeley National Laboratory (LBNL) using linearly-polarized photons of 61.0 eV to investigate the fragmentation dynamics of D_2O molecules. The photon energy resolution was set to approximately 200 meV using the 10.0.1 monochromator[8]. As the fragmentation channel of interest is very rare, the photon energy of 61.0 eV was chosen to be near the maximum of the PDI cross section of D_2O. For this photon energy, electrons with kinetic energies of up to 30 eV are generated and detected with full solid angle and adequate energy resolution ($\Delta E/E \approx 0.1$). In our experiment the electron sum energy is greater than 5 eV, which is helpful in utilizing a large region of the 3D electron pair detection phase space, minimizing losses due to the electron-pair detector dead-time[9].

The experimental setup was similar to the one described in Ref.[4]. In brief, a supersonic gas jet consisting of preheated D_2O vapour with a stagnation pressure of 2 bar was formed by heating the nozzle, the gas line, and the D_2O reservoir to temperatures of 125°C, 115°C, and 105°C, respectively. The supersonic gas jet was collimated laterally by a set of two skimmers (of 0.3 and 0.5 mm orifice diameters) and was then crossed with the photon beam inside the 3D momentum particle imaging spectrometer of a reaction microscope, a.k.a. COLd Target Recoil Ion Momentum Spectroscopy (COLTRIMS) apparatus[10–12]. A static electric field of 12.2 V/cm and a parallel magnetic field of 10.2 G guided electrons and ions to two micro-channel plate detectors, each equipped with delay line readout[9,13], which were located at the opposite ends of the spectrometer. Electrons of up to 30 eV and ionic fragments of up to 22 eV could be collected with 4π solid angle.

The time-of-flight (TOF) and position-of-impact (POI) of two ionic fragments and two electrons were detected in coincidence and processed in an intricate offline analysis, which included the cleaning, sorting, and calibrating of the list-mode file data. The data-set was reduced to coincidence events containing two cations plus two electrons via placing software restrictions on the PhotoIon-PhotoIon Coincidence (PIPICO) TOF spectra and the electron-ion energy correlation diagrams. Employing D_2O as a target molecule enabled us to distinguish between PDI events from any residual H_2O background present in the vacuum chamber ($\approx 1.2 \times 10^{-8}$ Torr) and the supersonic gas jet in the PIPICO TOF spectrum (not shown here). Moreover, the electric extraction field and spectrometer geometry were optimized to ensure that there was no overlap between the $D^+ + O^+ + D$ channel and the neighboring $OH^+ + D$ and $OD^+ + D^+$ two-body breakups in the PIPICO TOF spectrum, and, hence, the reaction channel of interest could be well isolated for further analysis. The 3D momentum vectors of the ions and electrons were calculated using the recorded POIs and TOFs of the respective particles. The momenta of the neutral fragments were then deduced using momentum conservation. The electron energy resolution $\Delta E/E$ is on the order of 10%. The average momentum resolution of O^+ ions is about ± 1.9 a.u., while the resolution of D^+ ions is around ± 0.7 a.u. As the derived momentum of the neutral D fragment is only on the order of 9.3 a.u., its resolution of about ± 2.3 a.u. has a large impact on the corresponding angular distributions in the lab and molecular frames.

3 Results & Discussion

3.1 Electron & Ion Energies

It is generally the case for small molecules that their Vertical Double Ionization Potentials (VDIPs) lie above the dissociation limits corresponding to singly-charged fragments. This is simply a consequence of the long-range Coulomb repulsion between singly-charged ions, which results in barriers to direct dissociation on the potential surfaces of molecular dications near the Franck-Condon region. This in turn leads to the possibility of populating metastable singly-charged ions by one-photon ionization at energies, generally below the ground-state of the dication, but above the asymptotic dissociation energies of the charged fragments. Consequently, IDI can then be the result of the autoionization of a neutral fragment at large internuclear separations where the excited monocation state crosses into the electron + dication continuum. This process was first observed in water by Winkoun *et al.* [14] and subsequently in other molecules including CO[15], O_2[16], and H_2S[17]. In the following we identify, isolate, and quantify such a super-excited state in the IDI of water molecules upon single-photon absorption (61 eV).

3.1.1 Experimental Results

We present the measured yield of the $D^+ + O^+ + D$ breakup after PDI of deuterated water molecules at 61 eV as a function of the Kinetic Energy Release (KER) and the kinetic energy E_{e_1} and E_{e_2} of either emitted electron e_1 and e_2 in Fig. 1(a). This electron-ion energy-correlation map probes the potential energy surface (PES) as it correlates the vertical transition after photoabsorption in the Franck-Condon (FC) region with the dissociation limit (KER) of the molecule (according to: $h\nu = E_{e_1} + E_{e_2} + \mathrm{KER} + \mathrm{VDIP}$). The diagonal line marks the maximum available excess energy of the experiment constrained by energy conservation ($h\nu$-$V_{D_2O} - IP_D - IP_O = 24.268$ eV, where $V_{D_2O} = 9.512$ eV is the dissocia-

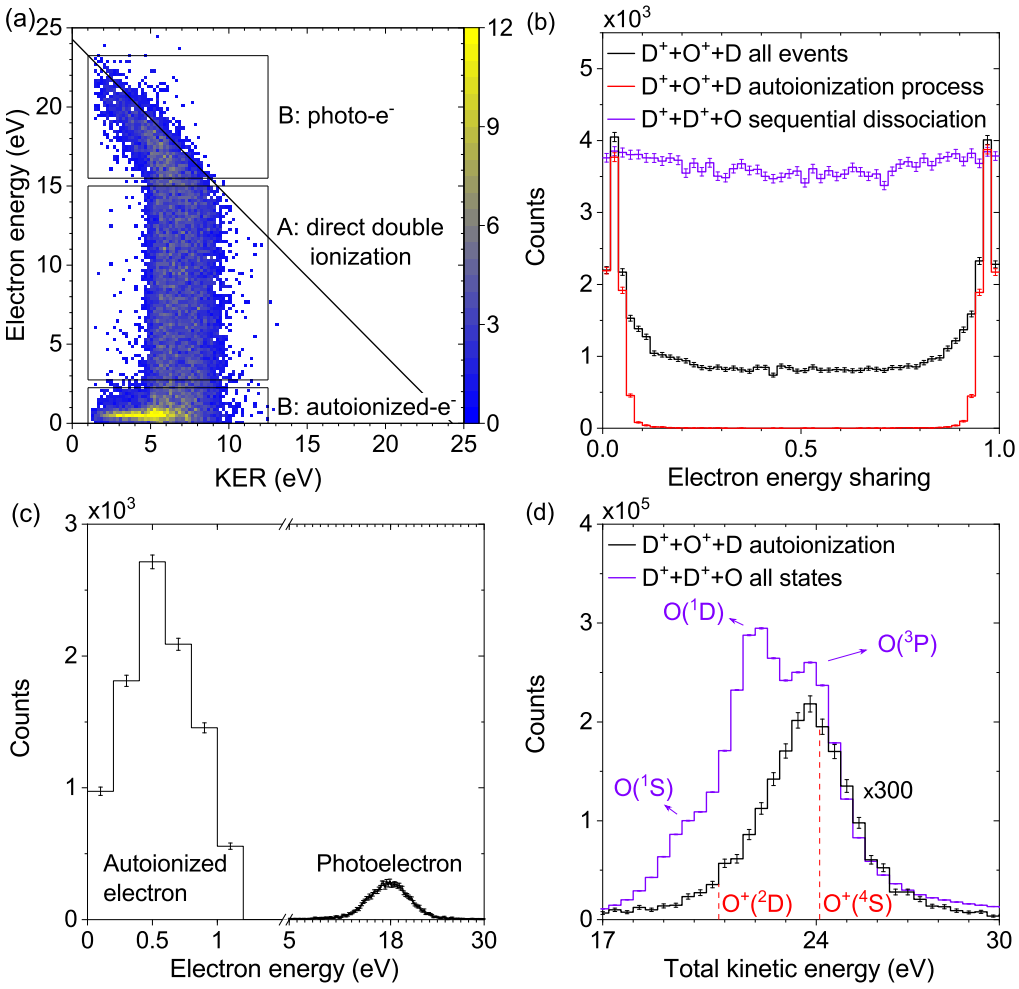

Fig. 1 (a) Photo-double ionization (PDI) yield of the $D^+ + O^+ + D$ breakup as a function of the kinetic energy release (KER) and the kinetic energy of either emitted electron, showing the direct double ionization (region A) and the autoionization contribution (regions B). The diagonal line indicates the boundary of the region of valid events constrained by energy conservation. (b) Electron energy sharing $E_{e_1}/(E_{e_1}+E_{e_2})$ of the PDI for all events (black line) and for the autoionization events only (red line) leading to $D^+ + O^+ + D$, and for the events of the $OD^+ + D^+$ sequential dissociation (purple line) leading to $D^+ + D^+ + O$. (c) Kinetic energy of either emitted electron in the PDI of D_2O leading to the $D^+ + O^+ + D$ fragmentation channel for the autoionization process showing the photoelectron e_P at high energy and the autoionized electron e_A at low energy. The abscissa is broken into two sections, $0-1.5$ eV and $5-30$ eV, to highlight the low-energy autoionized electron (we note that the two intervals use the same binning but are shown in different aspect). (d) Total kinetic energy ($E_{e_{P_1}} + E_{e_{P_2}} + KER$) for the direct double ionization of D_2O leading to the $D^+ + D^+ + O + 2\,e_P$ breakup (purple line) and ($E_{e_P} + E_{e_A} + KER$) for the autoionization process (black line) leading to the $D^+ + O^+ + D + e_P + e_A$ breakup. The vertical red dashed lines indicate the expected energy of each $D^+ + O^+ + D$ dissociation limit and are labeled with the final state of O^+. All error bars represent one standard deviation in the statistical uncertainty.

tion energy needed to fully atomize D_2O, IP_D = 13.602 eV, and IP_O = 13.618 eV). Moreover, we can also see how the two emitted electrons e_1 and e_2 are correlated. We can deduce that there are two distinct processes leading to the fragmentation channel under investigation: (A) direct PDI and (B) single ionization plus excitation followed by autoionization. The two contributions (A) and (B) are separated according to their available excess energies, which depend on the photon energy and the ionic states involved. This can be clearly seen as two distinct features in Fig. 1(a). The direct double ionization process (A) represents the scenario in which two electrons e_1 and e_2, which are indistinguishable, are emitted simultaneously. Here, the two electrons share their kinetic energy continuously, which manifests as the vertical stripe at KER between $\approx 5-9.5$ eV in Fig. 1(a). In the autoionization process (B), the two electrons are emitted separately in two steps. In this sequence the photoelectron e_P and autoionized electron e_A show no correlation; each electron exhibits its own kinetic energy distribution in this electron-ion energy map. The electron-ion energy correlation map exhibits a fast photoelectron (high-energy diagonal feature) and a slow autoionized electron (narrow low-energy horizontal feature).

The two contributions (A) and (B) are also visible in the electron energy sharing $E_{e_1}/(E_{e_1}+E_{e_2})$, depicted in Fig. 1(b) as the black line. The flat contribution ranging from 0 to 1 corresponds to the direct PDI (A), and the sharp peaks near 0 and 1 represent the slow autoionized electron and fast photoelectron of the autoionization process (B), respectively. By gating on these features, we are able to separate the two processes and investigate them, in order to identify the contributing states, the dissociation limits, and the dissociation pathways leading to the $D^+ + O^+ + D$ fragments. The red line shows the electron energy sharing for the autoinization process after requiring that one of the electrons yields a kinetic energy below 1.1 eV. The relative yield ratios between these two processes are around 76.9% for the direct double ionization process and 23.1% for the autoionization process with a relative error of less than 6% each. For comparison we also show the electron energy sharing leading to the sequential dissociation of the dominating $D^+ + D^+ + O$ channel in Fig. 1(b) as the purple line. In contrast to the $D^+ + O^+ + D$ channel, it shows a flat distribution, i.e., no sign of autoionization processes. We will make use of this observation later in section 3.1.2, when we identify the fragmentation process at play.

It is noteworthy to point out that, as the autoionization partly overlaps with the direct ionization, as seen in Fig. 1(a), the separation of the two processes is not perfect. The yield of the autoionization processes is polluted to a degree of around 25% by events from direct double ionization. This unwanted contribution affects events with KER between 5 – 9.5 eV. To minimize effects from this pollution in the analysis of the autoionization processes presented in this work, we thus selected events with KER < 5 eV for all following experimental spectra except for Fig. 1(a,b,c); comparison of data with and without this KER gate showed that this restriction did not result in the omission of any characteristic features in Fig. 1(d) (or in Fig. 4 to Fig. 7, discussed later) but did cause small shifts in the displayed energy distribution of the photoelectrons in Fig. 1(c). The investigation of the direct double ionization process can be found in Ref. [18].

The kinetic energies E_P and E_A of the detected electrons from the autoionization process are presented in Fig. 1(c). The energy of the autoionized electron E_A is centered around 0.5 eV, and the corresponding photoelectron energy is centered around 18 eV. The distribution of the photoelectron energy E_P corresponds to an average VDIP of 43 eV. That implies that the contributing states of the excited monocation D_2O^{+*} for the autoionization processes are located ≈ 4 eV above the double ionization threshold of D_2O, which is around 39 eV [19].

Within our resolution, for the autoionized electron, the kinetic energy E_A is represented by a very narrow distribution, which distinctly peaks at the low value of 0.5 eV. Such a distribution usually is a signature of atomic autoionization, i.e., the photoexcited D_2O^{+*} ion dissociates into $D^+ + O^* + D$ and, subsequently, the excited O^* atom autoionizes with an emission of a low-energy electron e_A at large internuclear distances. In order to yield the measured narrow distribution in kinetic energy of the autoionized electron e_A, the autoionization process must be taking place when the fragments are well separated. Accordingly, a crossing between the $D^+ + O^* + D$ and $D^+ + O^+ + D$ PESs is necessary in order for the autoionization process to be energetically allowed. Given the measured momenta and assuming Coulomb potentials, i.e., 1/R potential energy curves (PECs), this crossing point is classically expected to be around 54 bohr, assuming the D_2O^{+*} curves to be flat at long distance.

The total kinetic energy distribution of the system, i.e., the sum of both electron energies and the KER, is presented in Fig. 1(d). It reveals that the autoionization process (black line) leading to $D^+ + O^+ + D$ fragments is correlated with a dissociative limit which is very close to the $D^+ + D^+ + O(^3P)$ fragmentation limit (purple line), which is also shown in Fig. 1(d). I.e., our coincidence experiment allows for a direct comparison of the total energy distributions of the $D^+ + D^+ + O$ and $D^+ + O^+ + D$ channel and, thus, enables us to experimentally identify the dissociation limit of the latter. We also see that in contrast to the $D^+ + O^+ + D$ channel driven by autoionization, the $D^+ + D^+ + O$ channel, which is initiated by direct double ionization, reveals three dissociation limits. We can conclude that the measured total kinetic energy is correlated with solely the $D^+ + O^+(^4S) + D$ limit, which is slightly higher than the $D^+ + D^+ + O(^3P)$ limit by a few meV [20,21]. This is well below the next nearest dissociation asymptote of $D^+ + O^+(^2D) + D$, which is estimated to be 3.3 eV higher in potential energy. As discussed in our previous investigation on the PDI of water (see Supplementary Note 2 in Ref. [22]), we point out here that the accumulated variance in the measured total kinetic energy distribution and photon energy, as well as the uncertainties in the complete dissociation energy of water recommended by NIST, add up to an estimated tolerance, which is on the order of the apparent small energy offset in the measured spectrum shown in Fig. 1(d) with the $D^+ + O^+(^4S) + D$ limit (vertical red dashed line).

In order to identify the electronic state of the excited O^* fragment before its autoionization, we have calculated the thermochemical thresholds for creating $D^+ + O^* + D$ fragments for several photoexcited oxygen states and present them in Ta-

Table 1 Dissociation products of the D_2O monocation and dication, thermochemical thresholds for the generated products, energy differences with respect to the lowest dissociation limit $D^+ + O^+(^4S) + D$ [23], and restrictions regarding the atomic transitions between O^* and $O^+(^4S)$

Fragmentation	Thermochemical Threshold (eV)	Energy Difference (eV)	Restrictions
$D^+(^1S) + O(^3P) + D^+(^1S)$	36.86	-0.02	
$D^+(^1S) + O^+(^4S) + D(^2S)$	36.88	0.00	
$D^+(^1S) + O^*(^2D3p)^1P + D(^2S)$	37.29	0.41	spin-orbit coupling
$D^+(^1S) + O^*(^2D3p)^3D + D(^2S)$	37.30	0.42	ΔL forbidden
$D^+(^1S) + O^*(^2D3p)^3F + D(^2S)$	37.36	0.48	ΔL forbidden
$D^+(^1S) + O^*(^2P3s)^3P + D(^2S)$	37.38	0.50	
$D^+(^1S) + O^*(^2D3p)^1F + D(^2S)$	37.39	0.51	ΔL forbidden
$D^+(^1S) + O^*(^2D3s)^1P + D(^2S)$	37.63	0.75	spin-orbit coupling
$D^+(^1S) + O^*(^2D3p)^1D + D(^2S)$	37.72	0.84	ΔL forbidden

ble 1. These are compared to the $D^+ + O^+(^4S) + D$ dissociation limit (second row). We conclude that the fragmentation into $D^+(^1S) + O^*(^2P3s)^3P + D(^2S)$ is the most probable intermediate state in this dissociation. The excited atomic fragment $O^*(^2P3s)^3P$ eventually autoionizes to $O^+(^4S) + e_A^-$ by emitting the measured low-energy (0.5 eV) electron, as shown in Table 1. All other products listed in Table 1 cannot be generated either due to angular momentum conservation requirements [i.e., they are ΔL forbidden according to the selection rules of the atomic transition between O^* and $O^+(^4S)$] or they demand spin-orbit coupling in the oxygen fragment, which is very unlikely.

3.1.2 Theoretical Results

In carrying out calculations to aid in the interpretation of the present experiment, we have been guided by our previous studies of indirect autoionization in CO [24] and H_2O [5] molecules. By analogy, we expect to find that single-photon EUV absorption can produce highly excited molecular monocations that subsequently dissociate and autoionize. We recall that the electronic configuration of neutral water is given as $1a_1^2\ 2a_1^2\ 1b_2^2\ 3a_1^2\ 1b_1^2$. The $2a_1$ orbital of water basically resembles the O(2s) shell and has a binding energy of ≈ 36 eV. Consequently, the removal of an inner-valence $2a_1$ electron can produce H_2O^+ ions with energies only a few eV below that of the water dication. However, in contrast to earlier studies [5,14], the present experiment measures the production of H_2O^+ well above the water dication threshold, which points to a scenario more involved than a single $2a_1$ electron removal. The lowest excited state of water is a $^3B_1$ neutral state, formed by promoting a $1b_1$ electron to $4a_1$, which lies ≈ 7 eV above the ground-state. The $4a_1$ orbital has Rydberg O(3s) character. A one-photon inner-valence excitation-ionization process that removes a $2a_1$ electron and simultaneously promotes a $1b_1$ electron to $4a_1$ would require ≈ 36 + 7 = 43 eV, consistent with our measurements of photoelectrons with an average energy of 18 eV following the absorption of a 61 eV photon.

To test this hypothesis, we carried out a series of Multi-Reference Configuration Interaction (MRCI) calculations on H_2O^+ and H_2O^{2+} ions for a series of geometries in which the two OH bonds were symmetrically stretched, keeping the HOH angle fixed at the equilibrium angle, 104.5°, of the neutral molecule. We began with a Self-Consistent Field (SCF) calculation on the water monocation. To ensure proper dissociation to ground-state products at infinity [i.e., $O^+(^4S) + H(^2S) + H(^2S)$], the SCF calculation was run in $^6A_1$ symmetry. This was followed by a Complete Active Space (CAS) plus single- and double-excitation Configuration Interaction (CI) procedure, from which state-averaged natural orbits were extracted, averaging over the three lowest roots. The final MRCI calculations were performed in $^2B_1$ symmetry at the CAS plus singles and doubles level, restricting the lowest O(1s) orbital to double occupancy and including seven orbitals in the active space. This generates roughly half a million configurations for the CI calculation at each geometry, from which the lowest 35 roots were computed. The results of these calculations are shown in Fig. 2.

To gauge the accuracy of the calculations, we note that our computed vertical energy difference between neutral water and the lowest $^2B_1$ state of H_2O^+ is 12.43 eV, compared to the experimental value of 12.62 eV [25]. Our computed vertical energy difference between the H_2O^+ monocation and the lowest $^3B_1$ state of the water dication is 27.45 eV, which puts the VDIP at 39.88 eV, i.e. well within the range of measured values [5,14,19]. The asymptotic energies for the $O + H^+ + H^+$ and $O^+ + H + H^+$ three-body breakups were extrapolated from the values calculated at an O – H distance of 20 bohr. They amount to 36.72 eV and 36.5 eV, respectively, which incorrectly places the $O + H^+$ asymptote 0.22 eV above the $O^+ + H$ dissociation limit rather than 0.02 eV below.

At the equilibrium geometry of neutral water, we find a super-excited monocation state at 5.6 eV above the ground-state of the dication. Its principal configuration is $2a_1 1b_1 4a_1$, $^2B_1$, giving it a mixed inner-valence/Rydberg character. The energy of the super-excited cation is seen to decrease precipitously as both O – H bonds are stretched from the initial geometry of neutral water, dropping below the energy of the dication at $O - H_{1,2} = 2.4$ bohr. Numerous crossings among the calculated H_2O^+ curves can be seen. To follow the super-excited ionic state through the maze of other ionic states, we examined the dominant CI coefficients of the roots at each geometry. We allowed states to cross if there was little interaction, but followed the adiabatic path otherwise [24,26]. When moving away from the Franck-Condon region, the super-excited state of H_2O^+ takes on an increasing Rydberg character and ultimately dissociates into $O^*(^2P3s)^3P + H + H^+$. At O-H separations greater than 20 bohr, the 2^3B_1 dication curve falls off as $1.0/|O\text{-}H|$. By extrapolating the dication curve, we estimate that O^* autoionization, which produces an $O^+(^4S)$ ion, can occur at O – H distances greater than 35 bohr (cyan solid line in Fig. 2),

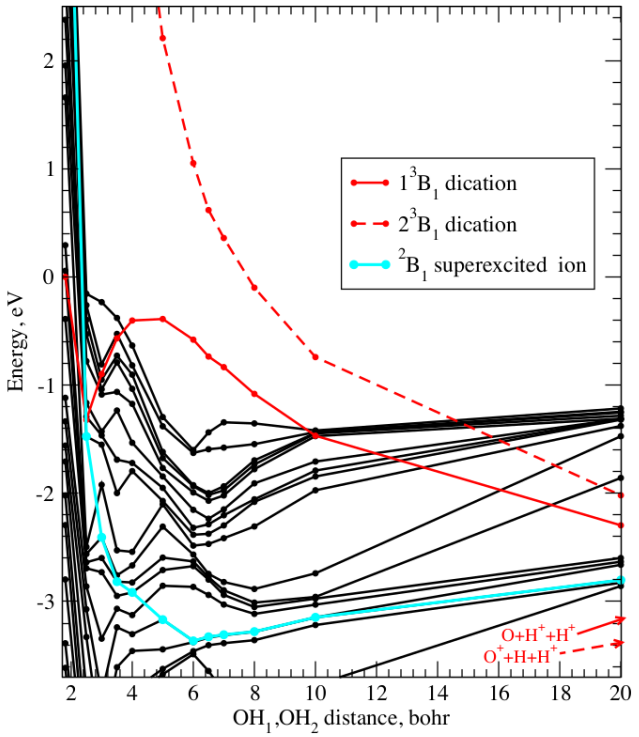

Fig. 2 Potential curves for the symmetric O−H stretch of H_2O^{+*} (solid black curves). The solid cyan line is the calculated diabatic representation of a super-excited H_2O^+ cation state with mixed inner-valence O(2s)/Rydberg character near the geometry of neutral water that correlates with the O^*+H+H^+ three-body breakup asymptotically. The solid red curve is the ground $^3B_1$ state of the water dication, and the broken red curve is the excited 2^3B_1 state of the dication. The zero of the energy scale is taken to be the ground-state of the dication at the equilibrium geometry of water. The dissociation limits of the three-body breakup are indicated at the right.

i.e., at a somewhat smaller R than the classically expected value in Sec. 3.1.1. If the calculated super-excited monocation and 2^3B_1 dication curves, the latter dissociating to $O^+(^4S)+H+H^+$, are extrapolated to infinite internuclear distances R, they are found to be separated by ≈ 0.6 eV, in reasonable agreement with the observed PEC spacing of 0.5 eV at large R, which is reflected by the kinetic energy of the measured autoionized electron. We performed an electron scattering calculation on isolated O^+ ions (not shown here), in order to estimate the lifetime of the autoionizing $O^*(^3P)$ state, which appears as a resonance in the elastic $e^-+O^+(^4S)$ channel. The resonance is extremely narrow and has a lifetime of around 25 ps.

The potential energy curves shown in Fig. 2 pertain to a direct three-body breakup to O^*+H+H^+. We should point out that although we held the HOH angle fixed at 104.5°, the excited cation energy shows a weak dependence on the bond angle, decreasing as the HOH angle increases (not shown here); we therefore expect an increase in the HOH angle during the fragmentation process or an asymmetric dissociation, with the H^+ escaping faster than the H, to produce a broader angular distribution of products for this three-body breakup.

We must emphasize that, starting with the initially created inner-valence/Rydberg excited monocation state, there are other dissociation paths on the same potential surface that can lead to the observed three-body final state. Another likely possibility is a sequential fragmentation, initiated by a fast ejection of H^+ followed by a subsequent autoionization of OH^* into O^++H. In the limiting case, where the OH^* fragment retains most of the internal energy as the H^+ ion escapes, the breakup could be characterized as a sequential process involving the OH^*+H^+ two-body breakup as a first step, followed by the dissociation and the autoionization of the neutral OH^* fragment into O^++H.

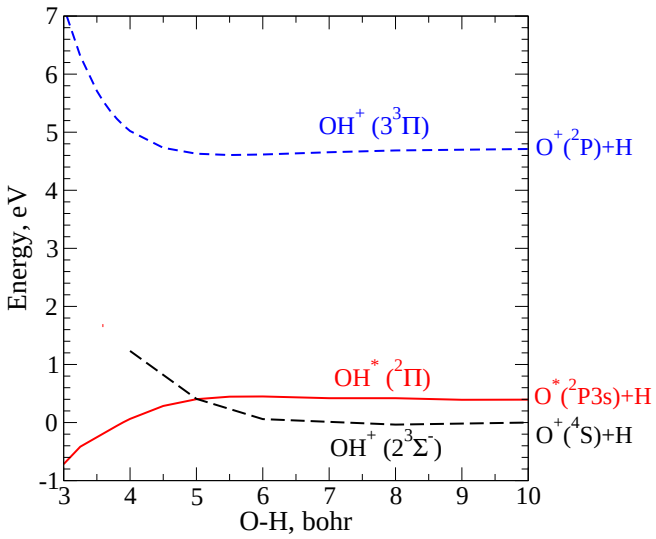

Fig. 3 Selected potential energy curves of OH^+ and OH^*. The autoionizing $^2\Pi$ state (red solid curve), whose parent ion (dashed blue curve) is the $3^3\Pi$ state of OH^+, can autoionize to the $OH^+(2^3\Sigma^-)+e_A^-$ continuum (dashed black curve) at bond lengths >5 bohr.

Consistent with the initial creation of an H_2O^{+*} monocation state by the excitation-ionization process described above, we examined autoionizing states of OH* that correlate with $O^*(^2P3s)^3P+H$, which produce electrons of ≈ 0.5 eV upon autoionization. These states must survive for several picoseconds to produce the observed autoionized electrons. The only parent ion triplet states of OH^+ that dissociate to $O^+(^2P)+H$ are the repulsive $3^3\Pi$ and the $1^3\Sigma^+$ states[27], which have similar potential curves. Since our codes cannot handle non-Abelian symmetries, we carried out MRCI calculations in $^2B_1$ symmetry. The results are shown in Fig. 3. By examining a series of discretized OH^* states, we were able to extract the diabatic resonance curve of interest (red solid line in Fig. 3). We note that the autoionizing $^2\Pi$ state is flat for O−H distances greater than 6 bohr and parallels the $OH^+(2^3\Sigma^-)$ state to which it can autoionize.

It is noteworthy that the present case, in which autoionization is observed in conjunction with O^+ production, contrasts sharply with what we previously reported in Sann *et al.*[5]. In that earlier study, photon absorption near the H_2O^{2+} threshold was found to result in indirect double ionization, where molecular autoionization from OH^* generated the reaction products of water, $OH^++H^++e_P+e_A$. The parent ions of these OH* autoionizing resonances previously observed in the two-body breakup were bound excited singlet states of OH^+, leading to a much broader energy distribution E_{e_A} of the autoionized electron e_A than in the

present case. For the three-body breakup discussed here, our calculations show a very low probability for molecular autoionization. The only possible OH^+ parents of the autoionizing OH^* fragment are strictly repulsive, and, therefore any OH^* transient dissociates quickly to $O^* + H$ reaching the flat section of the potential curve quickly. In this region on the potential energy landscape the transient fragment already stretched beyond a molecular bond, and consequently the autoionization is taking place in an isolated O^* atom.

This finding is supported from the experimental side. We did not detect any noticeable contribution from autoionization after PDI of D_2O^{2+} at 61 eV for the $D^+ + D^+ + O$ three-body fragmentation via sequential $OD^+ + D^+$ dissociation[22]. The measured electron energy sharing is mostly flat, shown as the purple line in Fig. 1(b), in contrast to the one shown as the black line, which depicts the electron energy sharing of the $D^+ + O^+ + D$ three-body breakup we report here. We can, hence, exclude molecular autoionization of OD^* from consideration as an alternative sequential dissociation pathway of the super-excited D_2O^{+*} monocation into $OD^* + D^+$ with subsequent breakup of OD^* into $O + D^+$, followed by a possible spin-orbit coupling to $O^+ + D$.

For completeness, we mention the option for H_2O^{+*} to dissociate into $OH^{+*} + H$, which then could possibly generate the detected reaction products $O^+ + H^+ + H$. PESs for this scenario are not yet available. However, *ab initio* calculations exploring even large geometry changes of the molecule found no OH^{+*} or OH^{2+} states in or near the Franck-Condon region that are non-repulsive or would support an autoionization process. The sequential dissociation scenario to $OH^{+*} + H$ as an intermediate is, hence, also removed from consideration.

3.2 Electron & Ion Emission Angles

To further unravel the dissociation dynamics leading to the $D^+(^1S) + O^*(^2P3s)^3P + D(^2S)$ fragmentation, we investigate the relative angles between the momenta of the nuclear fragments in the molecular breakup frame. While integrating over the direction of the polarization vector, this reference frame is defined by the measured momenta of the three heavy fragments in the laboratory frame, which establish a plane, since the momenta of the electrons are small. The motion of this reference frame is neglected when the momentum of the neutral D fragment is evaluated via momentum conservation. Relative azimuthal angles $\phi_{A,B}$ between the momenta of the fragments A and B are measured around the normal of this plane [via arctan(A/B)]. As discussed in Sec. 3.1.2, two possibilities for producing the same charged and neutral fragments in different dissociation sequences can be considered here (D_I denotes the firstly emitted D-fragment, while D_{II} represents the second emitted D-fragment):

$$h\nu + D_2O \rightarrow D_2O^{+*} + e^- \rightarrow$$

$$\text{(I)}: D^+ + D + O^* \rightarrow D^+ + D + O^+ + e^-$$

$$\text{(II)}: OD^* + D_I^+ \rightarrow D_{II} + O^* + D_I^+ \rightarrow D_{II} + O^+ + D_I^+ + e^-$$

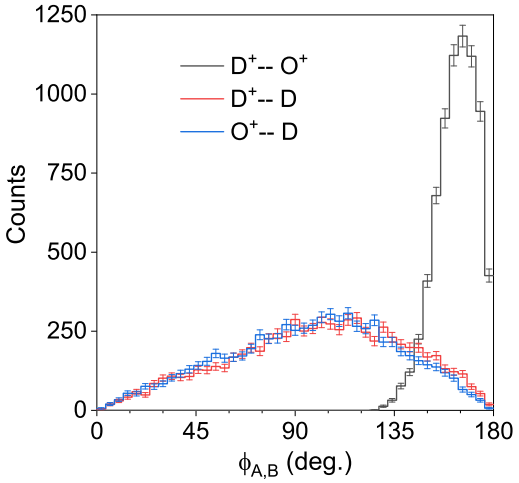

Fig. 4 Measured $D_{II} + O^+ + D_I^+$ autoionization yield (arb. units) as a function of the relative angle in the molecular frame, $\phi_{A,B}$ (see text), between fragment pairs D^+ and O^+ (black), D^+ and D (red), and O^+ and D (blue). All error bars represent one standard deviation in the statistical uncertainty.

The distribution of the relative dissociation angle $\phi_{D^+,D}$ between the D^+ ion and neutral D fragment for the direct three-body fragmentation (scenario I) is expected to be narrow due to the PESs, as seen in Ref.[4], with a width slightly larger than the relative angular resolution of $\phi_{D^+,D}$. The measured angle $\phi_{D^+,D}$, shown in Fig. 4 (red line), peaks around 108°. This peak value is very close to the bond-angle of the neutral water molecule of 104.5°. As pointed out in Sec. 3.1.2, we expect a rise in the HOH angle during the dissociation, which may explain the small increase in the peak value to 108° we observe experimentally. However, the distribution in Fig. 4 (red line) is notably wider than the resolution of the relative angle $\phi_{D^+,D}$. The latter is estimated to be around 23° for this fragment pair. We do not expect such a broad angular distribution between the charged and neutral fragments for a fast direct three-body breakup. This leads us to suspect that scenario I is not the only contributor to our data.

In the sequential breakup scenario (II), the near back-to-back emission of the two ionic fragments O^+ and D_I^+ (black line in Fig. 4) is plausibly grounded in the first breakup step on the PES, where the OD_{II}^* fragment receives considerable momentum opposite to the D_I^+ ion. This emission pattern is slightly amplified when the oxygen atom autoionizes and produces an O^+ ion, which interacts with the repulsive Coulomb potential of the far away D_I^+ fragment. Any rotation of the OD_{II}^* intermediate will mainly affect the emission angle of the neutral D_{II} fragment with respect to the $OD_{II}^* - D_I^+$ fragmentation axis. This is reflected in the broad relative angular distributions of the $D_I^+ - D_{II}$ (red) and $O^+ - D_{II}$ (blue) fragment pairs, as seen in Fig. 4.

We find additional evidence that the sequential dissociation scenario (II) is taking place by employing the native frame analysis[6,7]. In the native frame analysis we suppose that the fragmentation proceeds sequentially in two breakup steps: the first step is the breakup of D_2O^{+*} into $OD_{II}^* + D_I^+$ and the second step is the breakup of OD_{II}^* into $O^* + D_{II}$. While calculating the momen-

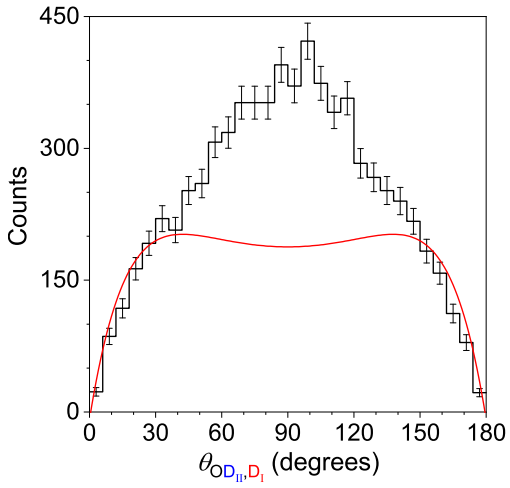

Fig. 5 Measured $D_{II}+O^+ + D_I^+$ autoionization yield (arb. units) as a function of the angle, θ_{OD_{II},D_I}, between the conjugate momenta of the first and second dissociation steps in scenario II evaluated using the native frame analysis (black line). Monte Carlo simulation of scenario II (red line). All error bars represent one standard deviation in the statistical uncertainty.

tum vectors of the fragments of the two breakup steps in Jacobi coordinates, we are able to analyze the dissociation angles of the assumed first breakup step and the final breakup step.

The measured angular distribution θ_{OD_{II},D_I} between the conjugate momenta of the first and second breakup steps in the native frames, shown in Fig. 5 (black line), is far from the expected isotropic emission pattern. However, the measurement of the relative angle θ_{OD_{II},D_I} is compromised by the poor momentum resolution of the deduced neutral D fragment in our experiment. In order to determine the impact of the poor momentum resolution on the measured θ_{OD_{II},D_I} angular distribution, we performed a Monte Carlo simulation on the two-body sequential fragmentation (scenario II). We first deduced the momenta of the three fragments upon dissociation from the measured KER associated with each step of the sequential breakup. We then sample θ_{OD_{II},D_I} randomly over the whole angular range, assuming the intermediate rotates longer than its rotational period in the fragmentation plane. The geometry of the spectrometer, the size of the interaction region, and the electric field applied to extract the fragments all the way to the detector have been implemented in the simulation. The spatial extent of the interaction region was simulated by generating randomly the initial position of single heavy water molecules, using a three-dimensional Gaussian distribution of FWHM(x, y, z) = (1.5, 1.9, 0.6) mm, corresponding to the overlap between the photon beam and the D_2O gas jet. The TOF and the POI of each simulated ion-pair on the detector were finally convoluted with the detector response function (POI and TOF resolution of, respectively, 0.25 mm and 0.5 ns) and recorded. The last step consisted of analyzing the simulated data using the same event sorting and filtering procedures as well as coordinate transformations that were used in analyzing the experimental data, including the native frame analysis.

The relative angle between the breakup axes of scenario II is sensitive to the measured momenta and assigned KERs of the detected fragments in the respective dissociation steps. The simulation of that angle shows that the modeled θ_{OD_{II},D_I}, which is presented in Fig. 5 (red line), deviates from an ideal flat distribution, visualizing the effects of the experimental resolution. However, while the minima at 0° and 180° are well reproduced, the simulated spectrum does not fully explain the shape of the measured angular distribution (black line), which exhibits a peak at 90°. This finding leads us to conclude that both, direct three-body fragmentation (scenario I) and two-body sequential fragmentation (scenario II) are contributing to the autoionization process.

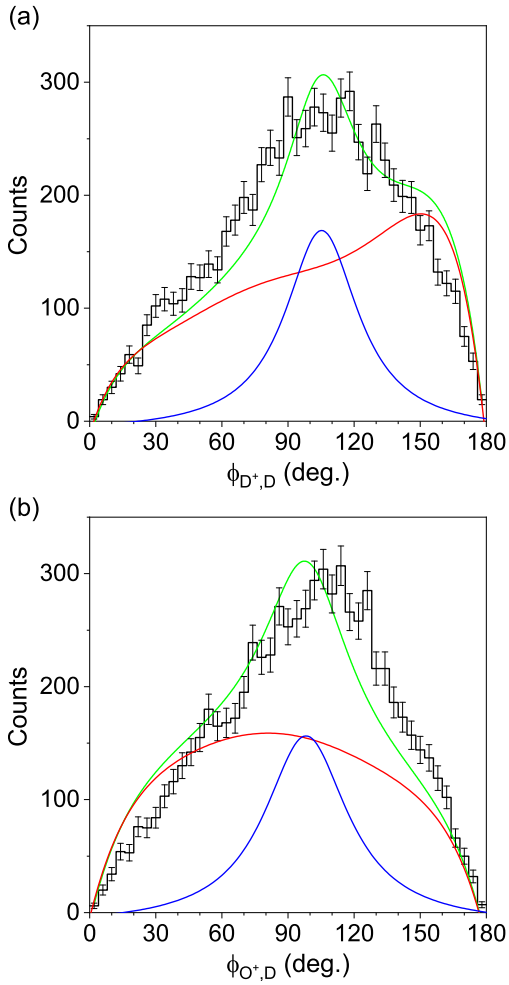

Fig. 6 Measured $D_{II}+O^+ + D_I^+$ autoionization yield (arb. units) as a function of the relative angle in the molecular frame (a) between the fragment pairs D^+ and D (black) and (b) between the fragment pairs O^+ and D (black). Monte Carlo simulation of fragmentation scenario I (direct: blue line), II (sequential: red line), and the fitted weighted sum (see text) of both scenarios (green line). All error bars represent one standard deviation in the statistical uncertainty.

In order to determine the contributions from each of the two fragmentation scenarios I and II to the measured distributions, we performed a similar simulation for the direct three-body fragmentation (scenario I). We first computed the momenta of the three fragments upon dissociation, using the measured kinetic energy associated with each fragment. The relative angle between D^+

and D was fixed at the bond-angle of the neutral water molecule of 104.5°. Similar to the simulation of scenario II, the spatial extent of the interaction region as well as the POI and TOF resolution of the detector for the two ions were included in the modeling. To determine the branching ratio of scenario I and scenario II, we used the relative angle between the momenta of the fragments D^+ and D, as shown in Fig. 6(a). The simulation for scenario I (blue line) shows a maximum at around 104.5° with a standard deviation of 23° related to the poor resolution of the neutral D fragment. The simulation for scenario II (red line) spans a wide range of angles due to the assumption that $OD_{II}{}^*$ rotated longer than the rotational period of the intermediate fragment ion between the two steps. Similar to the discussion of ϕ_{D^+,O^+} in Fig 4 above, the peak in $\phi_{D^+,D}$ around 150° for scenario II is due to the momentum of the neutral D_{II} fragment being governed by the back-to-back emission of the two strongly repelling fragments in the first step, i.e., the $OD_{II}{}^* + D_I^+$ breakup of the super-excited D_2O^{+*} cation. The fit (green line) of the experimental data, consisting of the sum contribution of the simulation of scenario I (blue line) and scenario II (red line), shows a good agreement with the measured data. From the fit we obtained a branching ratio of 28% ± 4% for scenario I and 72% ± 5% for scenario II. The agreement of the simulation with the measurement is the same when comparing the relative angles between the other fragments, e.g., O^+ and D, as shown in Fig. 6(b).

For completeness we state the asymmetry of the emission patterns of the heavy fragments in the laboratory frame, i.e., with respect to the linear polarization axis of the incoming light for both cases, direct and sequential fragmentation. The ionic fragments O^+ and D^+ exhibit rather isotropic angular distributions with asymmetry parameters of $\beta(O^+)$ = -0.2 ± 0.03 and $\beta(D^+)$ = -0.08 ± 0.03, respectively. On the other hand, the neutral D fragment is emitted preferentially along the perpendicular direction to the polarization vector with an asymmetry parameter of $\beta(D)$ = -0.76 ± 0.04.

Figure 7 shows the angular distribution of the emitted photoelectron with respect to the polarization axis of the incoming light. The emission pattern resembles a spherical harmonic with d- or f-wave (m = [0, 1]) character. This reflects the photoionization of innershell orbitals as opposed to the emission from valence orbitals in the direct PDI of water at the same photon energy resulting in the $D^+ + O^+ + D$ fragmentation, which yields a rather isotropic photoelectron angular distribution (not shown here). The details of the distribution are guided by the simultaneous $^1A_1$ photoionization and $1b_1$ to $4a_1$ excitation of the D_2O^{+*} monocation. To maintain overall (photoelectron plus ion) $^1B_1$ symmetry, the photoelectron emission from an O(2s) orbital is, hence, expected to mainly exhibit s-wave character. The observed higher angular momentum contributions are likely attributable to scattering of the outgoing electrons at the hydrogen atoms.

The emission pattern of the autoionized electron with energies between 0 and 1.1 eV was found to be isotropic with respect to the polarization vector as well as to any of the O – D axes for all KERs (not shown here). The latter is in contrast to our previous PDI measurements on water at 41 eV in Sann *et al.*[5], which investigated autoionization leading to the $OH^+ + H^+$ two-body breakup and found a strong asymmetric electron emission pattern in the $OH^* - H^+$ frame, which was due to Rutherford scattering between the autoionized electron and the proton, resulting in an appreciable flux of the autoionized electrons towards the H^+ ion. This is apparently not the case in the PDI experiment at 61 eV presented here.

The energy distribution of the autoionized electron, depicted in Fig. 1(c), is notably sharp and points to only the super-excited $^2B_1$ ionic state of water being populated rather than a mix of states, as seen in the broader electron energy distribution in the PDI at 41 eV (compare to Fig. 2 in Sann *et al.*[5]), which contained several resonances with lifetimes ranging from a few picoseconds down to 50 femtoseconds. Consequently, the autoionization of the super-excited $^2B_1$ ionic state appears to have a larger lifetime than the extracted autoionization decay time of around 2 ps in Sann *et al.*[5]. In order to yield an isotropic angular distribution for the autoionized electron in the molecular frame, i.e., show negligible influence of Rutherford scattering on the deuteron, the decay at either $OD_{II}{}^* - D_I^+$ (sequential dissociation) or $O^* - D^+$ (direct fragmentation) distances must take place at values greater than 2000 bohr. E.g., extending the classical scattering simulations from Sann *et al.*[5] [see details and Fig. 4(c) in Ref.[5]] to higher $O^* - D^+$ distances shows that the electron flux towards the D^+ fragment, which results in an anisotropic angular distribution, drops below 1% for R = 2300 bohr already for electron energies as low as 0.05 eV (see Fig. 8). For an average KER of around 4.5 eV, the minimal distance of 2000 bohr corresponds to a minimal time delay of ≈ 4.7 ps between the emission of the photoelectron e_P and the autoionized electron e_A for the direct three-body breakup (scenario I) in which the O^+ has 0.46 eV, D^+ has 3.65 eV, and D has 0.36 eV of kinetic energy on average. For the sequential dissociation (scenario II), in which 4.1 eV was released between the OD^* and the D^+ fragments and 0.4 eV was released between the O^* and D fragments, we deduce a minimal lifetime of 4.8 ps. This is ≈ 5 times shorter than the calculated $O^*(^3P)$ lifetime of around 25 ps in Sec. 3.1.2.

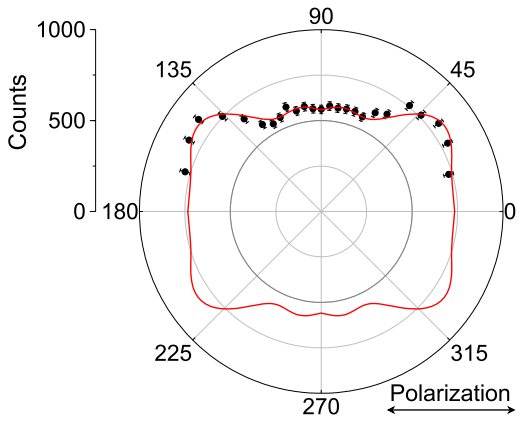

Fig. 7 Angular distribution of the photoelectron with respect to the polarization axis (horizontal) in the autoionization process leading to D_2O^{+*} at 61 eV. The (red) line depicts a fit to the data points with spherical harmonics containing Legendre polynomials up to the fourth-order (l = [1, 4], m = [0, 4]). All error bars represent one standard deviation in the statistical uncertainty.

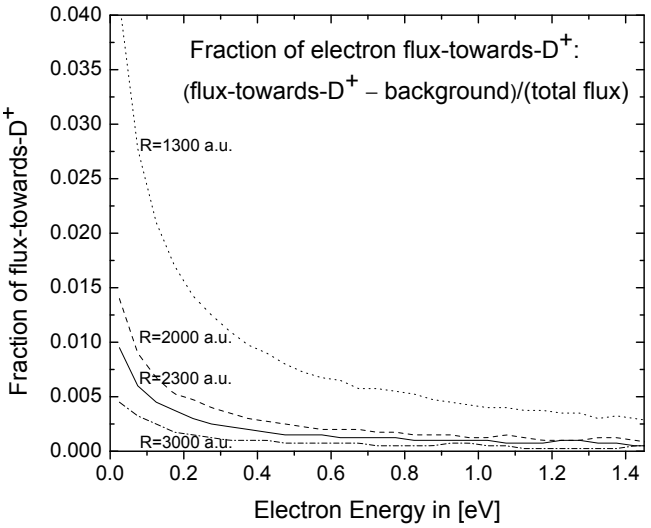

Fig. 8 Ratio of the electron flux towards the D^+ fragment (after subtraction of the isotropic background) and the total flux in 4π as a function of electron energy for the dissociation of $O^* - D^+$. Lines: classical scattering simulation for electron emission at different R between the O^* and D^+ (from top to bottom: R = 1300, 2000, 2300, and 3000 a.u.). Adapted from Sann et al.[5].

4 Conclusions

In summary, by applying reaction microscopy we were able to identify and isolate the $D^+ + O^+ + D$ dissociation channel of deuterated water after single-photon double ionization using 61 eV synchrotron light pulses. This breakup is extremely rare (0.7% of all PDI events). Around 77% of these scarce events where produced via direct photo-double ionization. About 23% stem from autoionization in which the $^2B_1$ super-excited D_2O^{+*} monocation state, around 4 eV above the double ionization threshold of D_2O, is populated and a 0.5 eV autoionized electron is emitted. This super-excited D_2O^{+*} monocation state lies 5.6 eV above the D_2O^{2+} dication at equilibrium geometry of the water molecule and correlates with the three-body $D^+ + O^*(^3P) + H$ dissociation limit. Our calculations indicate that the $^2B_1$ super-excited water monocation state is generated by removing an inner valence $2a_1$ O(2s) electron and simultaneously exciting an electron from the $1b_1$ to the $4a_1$ orbital.

In the majority of the autoionization events (72%) the super-excited deuterated water monocation first dissociates into $OD_{II}{}^* + D_I^+$ and subsequently to $D_{II} + O^*(^2P3s)^3P + D_I^+$, followed by the atomic autoionization of $O^*(^2P3s)^3P$, which finally produces the detected $D_{II}(^2S) + O^+(^4S) + D_I^+(^1S)$ three-body breakup. A smaller fraction of events (28%) fragment directly into the three-body channel $D + D^+ + O^*$, followed by the autoionization of the atomic oxygen.

On the experimental side we found that the minimal internuclear distance for autoionization of the isotropically emitted O^* fragment to set in is $\geq$ 2000 bohr, corresponding to an estimated time delay of at least 5 ps between the photoionization and the atomic decay. Theory predicts an even longer time delay of ca. 25 ps for a 0.6 eV autoionized electron to be emitted isotropically from the decaying atomic O^* fragment. By all means, the creation of the super-excited radical D_2O^{+*} cation, which dissociates promptly into three fragments either directly or sequentially, results in a long-lived $O^*(^3P)$ fragment that can act as a destructive carrier, traveling long distances before it releases its low-energy electron that can attach to neighboring molecules in the environment and initiate secondary reactions such as breakup of DNA strands – a key radiation damage mechanism.

Data Availability

The data-sets generated during the current study are available from the corresponding authors upon reasonable request.

Author Contributions

W.I. and Th. W designed the experiment. W.I., Th. W., K.A. L, B.G., J.B. W., D. C., V. D., B. J., T. S., and D.S. S. conducted the beam time and acquired the experimental data. W.I. analyzed the data. T.N. R. and A.E. O. performed the theoretical calculations. W.I., T.N. R, and Th. W. wrote the manuscript with significant review and editing by I. B-I., D.S. S.and K.A. L, which all co-authors approved. A.E. O., W.I., Th. W., and T.N. R. created the figures.

Conflicts of Interest

There are no conflicts to declare.

Acknowledgments

We thank T. Weinacht for sparking our interest in this scarce water fragmentation channel. We thank R. Dörner for providing the simulation code from Sann et al.[5]. We thank C.W. McCurdy, R. Lucchese, and Z. Streeter for helpful discussions. Work at LBNL was supported by the U.S. Department of Energy (DOE), Office of Science, Basic Energy Sciences (BES) under Award No. DE-AC02-05CH11231. This research used resources of the Advanced Light Source (ALS) and the National Energy Research Scientific Computing Center (NERSC), both being DOE Office of Science User Facilities under contract No. DE-AC02-05CH11231. In particular we acknowledge NERSC award BES-ERCAP-0020143 (theory) and BES-ERCAP-0019776 (experiment). We thank the staff of the ALS, in particular beamline 10.0.1 for their outstanding support. The JRML personnel was supported by the U.S. Department of Energy (DOE), Office of Science, Basic Energy Sciences (BES) under Award No. DE-FG02-86ER13491. UNR personnel acknowledges support from the National Sciences Foundation under Award No. NSF-1807017 and NSF-2208017. We are indebted to the Roent-Dek Company for long-term support with detector software and hardware.

Notes and References

1 M. Yoshimura, S. Itasaka, H. Harada and M. Hiraoka, *BioMed Res. Int.*, 2013, **2013**, 685808.

2 M. Blanc, D. J. Andrews, A. J. Coates, D. C. Hamilton, C. M. Jackman, X. Jia, A. Kotova, M. Morooka, H. T. Smith and J. H. Westlake, *Space Sci. Rev.*, 2015, **192**, 237–283.

3 E. Alizadeh, T. M. Orlando and L. Sanche, *Annu. Rev. Phys. Chem.*, 2015, **66**, 379–398.

4 D. Reedy, J. B. Williams, B. Gaire, A. Gatton, M. Weller,

A. Menssen, T. Bauer, K. Henrichs, P. Burzynski, B. Berry, Z. L. Streeter, J. Sartor, I. Ben-Itzhak, T. Jahnke, R. Dörner, T. Weber and A. L. Landers, *Phys. Rev. A*, 2018, **98**, 053430.

5 H. Sann, T. Jahnke, T. Havermeier, K. Kreidi, C. Stuck, M. Meckel, M. S. Schöffler, N. Neumann, R. Wallauer, S. Voss, A. Czasch, O. Jagutzki, T. Weber, H. Schmidt-Böcking, S. Miyabe, D. J. Haxton, A. E. Orel, T. N. Rescigno and R. Dörner, *Phys. Rev. Lett.*, 2011, **106**, 133001.

6 J. Rajput, T. Severt, B. Berry, B. Jochim, P. Feizollah, B. Kaderiya, M. Zohrabi, U. Ablikim, F. Ziaee, K. Raju P., D. Rolles, A. Rudenko, K. D. Carnes, B. D. Esry and I. Ben-Itzhak, *Phys. Rev. Lett.*, 2018, **120**, 103001.

7 T. Severt, *PhD thesis*, Kansas State University, 2021.

8 Z. Ali, Y- D. Chuang, D. Kilcoyne, A. Aguilar, S-K. Mo and Z. Hussain, *Proc. SPIE Advances in X-Ray/EUV Opt.*, 2012, **8502**, 85020P.

9 O. Jagutzki, A. Cerezo, A. Czasch, R. Dorner, M. Hattas, M. Huang, V. Mergel, U. Spillmann, K. Ullmann-Pfleger, T. Weber, H. Schmidt-Bocking and G. Smith, *IEEE Trans. Nucl. Sci.*, 2002, **49**, 2477–2483.

10 R. Dörner, V. Mergel, O. Jagutzki, L. Spielberger, J. Ullrich, R. Moshammer and H. Schmidt-Böcking, *Phys. Rep.*, 2000, **330**, 95–192.

11 J. Ullrich, R. Moshammer, A. Dorn, R. Dörner, L. P. H. Schmidt and H. Schmidt-Böcking, *Rep. Prog. Phys.*, 2003, **66**, 1463–1545.

12 T. Jahnke, T. Weber, T. Osipov, A. Landers, O. Jagutzki, L. P. H. Schmidt, C. L. Cocke, M. H. Prior, H. Schmidt-Böcking and R. Dörner, *J. Electron Spectrosc. Relat. Phenom.*, 2004, **141**, 229–238.

13 R. Dörner, T. Weber, M. Achler, V. Mergel, L. Spielberger, O. Jagutzki, F. Afaneh, C. L. . Cocke and H. Schmidt-Böcking, in *Imaging in Chemical Dynamics (ACS Symposium Series)*, Oxford University Press, ch. 20, pp. 339–349.

14 D. Winkoun, G. Dujardin, L. Hellner and M. J. Besnard, *J. Phys. B*, 1988, **21**, 1385–1394.

15 P. Lablanquie, J. Delwiche, M.-J. Hubin-Franskin, I. Nenner, P. Morin, K. Ito, J. H. D. Eland, J.-M. Robbe, G. Gandara, J. Fournier and P. G. Fournier, *Phys. Rev. A*, 1989, **40**, 5673–5689.

16 S. D. Price and J. H. D. Eland, *J. Phys. B*, 1991, **24**, 4379–4389.

17 J. H. D. Eland, P. Lablanquie, M. Lavollée, M. Simon, R. I. Hall, M. Hochlaf and F. Penent, *J. Phys. B*, 1997, **30**, 2177–2186.

18 W. Iskandar *et al.*, *submitted to J. Chem. Phys.*, 2023.

19 J. H. D. Eland, *Chem. Phys.*, 2006, **323**, 391–396.

20 Z. L. Streeter, F. L. Yip, R. R. Lucchese, B. Gervais, T. N. Rescigno and C. W. McCurdy, *Phys. Rev. A*, 2018, **98**, 053429.

21 U. Hechtfischer, J. Levin, M. Lange, L. Knoll, D. Schwalm, R. Wester, A. Wolf and D. Zajfman, *J. Chem. Phys.*, 2019, **151**, 044303.

22 T. Severt, Z. L. Streeter, W. Iskandar, K. A. Larsen, A. Gatton, D. Trabert, B. Jochim, B. Griffin, E. G. Champenois, M. M. Brister, D. Reedy, D. Call, R. Strom, A. L. Landers, R. Doerner, J. B. Williams, D. S. SLaughter, R. R. Lucchese, Th. Weber, C. W. McCurdy and I. Ben-Itzhak, *Nat. Comm.*, 2022, **13**, 5146.

23 J. E. Sansonetti and W. C. Martin, *J. Phys. Chem. Ref. Data*, 2005, **34**, 1559–2259.

24 T. Osipov, T. Weber, T. N. Rescigno, S. Y. Lee, A. E. Orel, M. Schöffler, F. P. Sturm, S. Schössler, U. Lenz, T. Havermeier, M. Kühnel, T. Jahnke, J. B. Williams, D. Ray, A. Landers, R. Dörner and A. Belkacem, *Phys. Rev. A*, 2010, **81**, 011402.

25 S. Y. Truong, A. J. Yencha, A. M. Juarez, S. J. Cavanagh, P. Bolognesi and G. C. King, *Chem. Phys.*, 2009, **355**, 183–193.

26 M. A. Hayes and C. J. Noble, *J. Phys. B*, 1998, **31**, 3609–3619.

27 D. M. Hirst and M. F. Guest, *Mol. Phys.*, 1983, **49**, 1461–1469.